

# Hyperfine interactions and perturbation effects in the $B0_u^+(^3\Pi_u)$ state of $^{127}\text{I}_2$

Lisheng Chen, Wang-Yau Cheng,\* and Jun Ye

JILA, National Institute of Standards and Technology and University of Colorado, Boulder, Colorado 80309-0440

Received September 25, 2003; revised manuscript received November 28, 2003; accepted December 4, 2003

We report new measurements of the hyperfine spectra of  $B \leftarrow X$  transitions in the wavelength range 500–517 nm. Four effective hyperfine parameters,  $eqQ_B$ ,  $C_B$ ,  $d_B$ , and  $\delta_B$ , are determined for an extensive number of rovibrational levels spanning the intermediate region  $42 \leq v' \leq 70$  in the electronically excited  $B0_u^+(^3\Pi_u)$  state. Second-order perturbation accounts for most of the observed rovibrational dependence of the hyperfine interactions. In addition, it was found that, near vibrational levels  $v' = 57$ – $60$ , the  $1_g(^1\Pi_g)$  electronic state strongly perturbs the  $B$  state through rotational coincidence, leading to effects such as abnormal variations in the hyperfine parameters and strong  $u$ – $g$  mixing recorded for the transition  $P(84) 60$ – $0$ . Various perturbation effects in the  $B$  state identified so far are summarized. Also, the radial dependence of the hyperfine interactions was examined by removal of the vibrational average in the hyperfine parameters. © 2004 Optical Society of America

OCIS codes: 020.2930, 300.6390, 300.6460, 300.6190.

## 1. INTRODUCTION

High-precision measurement of hyperfine interactions in the  $^{127}\text{I}_2$  molecule over an extended range of rovibrational levels is valuable both for studying the molecular electronic structure and applying its rich spectrum to laser frequency stabilization. Because of the nonzero spin of the iodine nucleus, the electromagnetic interaction between the nuclear and surrounding charge distributions results in additional energy and subsequently in a hyperfine structure, forming the finest energy scale in the molecule. This seemingly weak effect has a subtle but noticeable influence on molecular structure. For instance, in the excited electronic state,  $B0_u^+(^3\Pi_u)$ , the lifetime variation over the hyperfine levels that belong to a single rovibrational level is a consequence of the state's predissociation to the  $B''1_u(^1\Pi_u)$  state through magnetic hyperfine coupling.<sup>1,2</sup> Another example of this effect is the hyperfine-induced  $u$ – $g$  mixing of the  $B0_u^+(^3\Pi_u)$  and  $1_g(^1\Pi_g)$  states that dramatically modifies the hyperfine structure at vibrational levels 76–78 in the  $B$  state.<sup>3,4</sup> Considering the broad scope within which the hyperfine effect operates, it is of great interest to examine the evolution of this effect with the progression of the vibrational levels toward the dissociation limit or, equivalently, with the stretch of the molecular bond from its equilibrium length to large internuclear separations, where a separated-atom model represents a good approximation to the molecular electronic wave function.

Hyperfine structures in the  $X0_g^+(^1\Sigma_g^+)$  and  $B0_u^+(^3\Pi_u)$  states have received extensive investigation through the prominent  $B \leftarrow X$  transition manifold in the visible and near-IR regions. By use of sub-Doppler detection schemes such as saturated-absorption spectroscopy and supersonic molecular beams, hyperfine spectra of  $B \leftarrow X$  transitions were measured for a large number of rovibrational levels with a precision that reached the ki-

lohertz level for each hyperfine component. Broyer *et al.* developed an effective Hamiltonian to describe the hyperfine interaction that can couple different electronic states.<sup>5</sup> Derived from this Hamiltonian are effective hyperfine parameters that characterize hyperfine coupling strength. Among those parameters, electric quadrupole ( $eqQ$ ), spin–rotation ( $C$ ), tensorial spin–spin ( $d$ ), and scalar spin–spin ( $\delta$ ) represent the four dominant parameters that have been widely used to analyze experimental spectra.

For the  $B$  state in  $^{127}\text{I}_2$ , perturbations from other electronic states can contribute significantly to various terms in the hyperfine Hamiltonian. Located above the  $B$  state on the molecular energy scale are a total of nine weakly bounded electronic states ( $0_g^+$ ,  $0_g^-$ ,  $0_u^-$ , two  $1_g$ , two  $1_u$ ,  $2_g$ , and  $2_u$ ),<sup>6–8</sup> which share the same  $^2P_{3/2} + ^2P_{1/2}$  dissociation limit with the  $B$  state. Furthermore, rovibrational levels in the  $B$  state are not far removed in energy from this cluster of states. As a result, these electronic states perturb the  $B$  state to various degrees through hyperfine coupling. Indeed, this qualitative estimate of the perturbation strength is confirmed by the observed global trend of a monotonic increase of the magnitude of the effective hyperfine parameters  $C_B$ ,  $d_B$ , and  $\delta_B$  along with the ascending vibrational level, a trend especially remarkable for those levels approaching the dissociation limit.<sup>9–12</sup> More quantitatively, for levels with vibration quantum numbers  $v' \leq 43$  the four-term effective Hamiltonian describes satisfactorily the hyperfine spectra with small residual errors ranging from a few tens to several kilohertz or even less,<sup>13</sup> indicating that in this region second-order perturbation is sufficient to account for the contributions from states other than the  $B$  state.

Moreover, hyperfine interaction in the region  $71 \leq v' \leq 82$  has been systematically investigated by Pique *et al.*<sup>3,4,14</sup> In addition to the second-order effect, strong

hyperfine perturbation from the  $1_g(^1\Pi_g)$  state was found at levels  $v' = 76, 77, 78$  owing to small energy differences and large Franck–Condon overlaps between the rovibrational levels in the  $B$  and  $1_g(^1\Pi_g)$  states. In particular, to deal with the strong perturbations at  $v' = 77$  and  $v' = 78$  requires that basis functions of the  $1_g(^1\Pi_g)$  state be included in the construction of the matrix that represents the effective Hamiltonian for the  $B$  state: A direct diagonalization of this new matrix gives the correct hyperfine spectrum. The resultant strong  $u$ – $g$  mixing was directly confirmed by the extra hyperfine lines recorded at the 78–0 bandhead.

Despite the fact that ample data were collected in the regions summarized above, covering the intermediate levels that spread from  $v' = 44$  to  $v' = 70$  will require more information. This is an important region for study of the  $^{127}\text{I}_2$  molecular structure because vibrational wave functions of these levels sample a relatively large range of internuclear separations. Direct hyperfine-spectrum measurements in this region have been made only for a limited number of transitions to which access is gained primarily by isolated laser lines such as 514.5- and 501.7-nm argon-ion laser wavelengths.<sup>15–17</sup>

Using a widely tunable and high-resolution spectrometer based on a frequency-doubled cw Ti:sapphire laser, we carried out systematic investigations of the hyperfine spectra of  $B \leftarrow X$  transitions in the wavelength range 500–517 nm and determined the detailed rovibrational dependence of the four effective hyperfine parameters in the region  $42 \leq v' \leq 70$ . In addition to the usual monotonic trend that results from the second-order effect, we observed strong perturbations at  $v' = 57$ –60. The source of this perturbation was confirmed, and its properties were studied. We also established a systematic dependence of the hyperfine interactions on internuclear separation  $R$ .

Besides these interesting studies of hyperfine structure, the narrow-linewidth  $\text{I}_2$  transitions in this wavelength range also provide excellent cell-based optical frequency references for laser frequency stabilization. Frequency-doubled Nd:YAG/ $^{127}\text{I}_2$  at 532 nm has been proved to be one of the best cell-based optical frequency standards because of its compact size, reliability, and high stability (with a fractional frequency instability of  $<5 \times 10^{-14}$  at 1 s).<sup>18</sup> To reach higher frequency stability it is useful to explore  $\text{I}_2$  transitions at wavelengths below 532 nm, where the natural linewidths can decrease at a faster rate than that for the line strengths. We measured the systematic variation of the  $\text{I}_2$  transition linewidths within the range 532–498 nm; the linewidth decreases by  $\sim 6$  times when the transition wavelength changes from 532 nm to near the dissociation limit.<sup>19,20</sup> The high signal-to-noise ratio for the recovered resonance information indicates that  $\text{I}_2$  transitions in the wavelength range 520–501 nm hold great promise for future development of optical frequency standards, especially with the advent of all-solid-state Yb:YAG lasers. One exciting candidate for such development is the 514.67 nm standard, with a projected instability of  $<1 \times 10^{-14}$  at 1 s. The  $\text{I}_2$ -based 532 nm optical standard has been used to stabilize an entire octave-bandwidth-spanning optical frequency comb based on a mode-locked Ti:sapphire laser,

thus establishing an optical atomic clock in which the rf signal is phase-coherently derived from the  $\text{I}_2$  optical transition.<sup>21</sup>

## 2. EXPERIMENT

A schematic of the experimental setup is depicted in Fig. 1. The system consists of a widely tunable frequency-doubled Ti:sapphire laser, a cell-based  $^{127}\text{I}_2$  spectrometer for saturated-absorption spectroscopy with the frequency modulation (FM) technique, and a self-referenced optical frequency comb<sup>22</sup> that makes the absolute-frequency measurement.

The Ti:sapphire laser is configured in a ring-cavity geometry with a set of long-wavelength (1- $\mu\text{m}$ ) coating mirrors and is pumped by a commercial diode-pumped solid-state laser at 532 nm. Laser intracavity components include an optical diode to enforce unidirectional operation, a birefringent filter for coarse wavelength adjustment, and a Brewster plate for fine frequency tuning. Two solid etalons with thickness of 0.5 and 10 mm are inserted into the laser cavity to facilitate single-mode operation. With these intracavity elements and 8 W of pump power, the output power of the Ti:sapphire laser is typically approximately 300 mW from 1000 to 1034 nm, with a moderate power drop at the long-wavelength end. Most of the laser radiation is sent to the frequency doubler through a pair of mode-matching lenses, and a small portion of the output power ( $\sim 15$  mW) is used for laser frequency stabilization.

To probe the narrow resonances of the  $^{127}\text{I}_2$  hyperfine spectra we use a reference cavity with fixed length to stabilize the Ti:sapphire's laser frequency. The cavity uses two highly reflective broadband mirrors (99%; a flat and a concave mirror with  $R = 1$  m), and its free spectral range and finesse are approximately 234 MHz and 200, respectively. The Zerodur cavity spacer is suspended inside an evacuated aluminum chamber that is temperature controlled to within 20 mK. To effectively isolate the cavity from vibrations of different origins we wrap the aluminum chamber with thermal insulation with lead foil interlayers, and three stages of damping structure are cascaded between the chamber and the optical table. The laser is tightly locked to one of the cavity modes by the Pound–Drever–Hall method by two feedback transducers: One is a piezoelectric transducer- (PZT-) activated cavity mirror and the other performs fast frequency correction with an acousto-optic modulator (AOM 1 in Fig. 1) located immediately following the output of the Ti:sapphire laser cavity. The linewidth of the stabilized Ti:sapphire laser has been verified by a heterodyne beat experiment with an independent narrow-linewidth laser to be less than 8 kHz.

Crucial to this high-resolution spectroscopy is precise and continuous scanning of the laser frequency over 1 GHz (a typical span of hyperfine spectra for one transition) without mode hop. The laser frequency, which is locked to the reference cavity, is scanned by a frequency synthesizer that drives a double-pass AOM (AOM 2 in Fig. 1) inserted between the laser and the reference cavity. The feedback signal applied to the PZT is in-



the published value of 131.7701(2) MHz.<sup>15</sup> Absolute-frequency measurement of any desired  $^{127}\text{I}_2$  transitions is facilitated by a self-referenced optical frequency comb based on a mode-locked femtosecond laser. Various system parameters, such as frequency and pressure shift, optical alignment, and residual amplitude modulation,<sup>23</sup> are characterized or optimized with the help of the optical frequency comb.<sup>22</sup> Whereas some of the hyperfine components have their absolute frequencies measured by the comb, most of the hyperfine-splitting measurements are carried out by the cavity based laser scan with its intrinsic frequency-calibrated scale coming from the frequency synthesizer that drives the AOM tuning element.

### 3. EFFECTIVE HYPERFINE HAMILTONIAN AND FITTING PROCEDURES

The hyperfine Hamiltonian in a homonuclear diatomic molecule with two nuclei, labeled  $a$  and  $b$ , and can be formally written as

$$H_{\text{hf}} = H_{\text{hf}}(a) + H_{\text{hf}}(b) + H_{\text{hf}}(a, b), \quad (1)$$

where  $H_{\text{hf}}(a)$  [ $H_{\text{hf}}(b)$ ] and  $H_{\text{hf}}(a, b)$  represent the nucleus–electron and nucleus–nucleus interactions, respectively. The fact that  $H_{\text{hf}}(a)$  and  $H_{\text{hf}}(b)$  can couple different electronic states was studied through the introduction of an effective hyperfine Hamiltonian.<sup>5</sup> This effective Hamiltonian acts only on one electronic state but has its matrix elements modified by second-order perturbation to take into account indirect hyperfine coupling with external electronic states. The advantage of this treatment is that, despite their different origins, various tensorial terms can be incorporated into a small set of effective hyperfine parameters according to their overall geometrical dependences evaluated with irreducible tensorial algebra, thereby simplifying the experimental analysis of hyperfine structure. The effective Hamiltonian can be summarized as

$$H_{\text{hf,eff}} = H_{eQq} + H_{\text{SR}} + H_{\text{TSS}} + H_{\text{SSS}} + H_e + H_f + H_h + H_{hH}, \quad (2)$$

where the four leading terms on the right-hand side represent major contributions from nuclear electric quadrupole, spin–rotation, tensorial spin–spin, and scalar spin–spin interactions, respectively. The last four terms arise primarily from second-order contributions not included in the four major terms and have been examined experimentally only for a few transitions without confirming evidence of their existence.<sup>15</sup> The matrix elements of these terms in electronic state  $\Omega$  (either the  $X$  or the  $B$  state) can be expressed as

$$\begin{aligned} \langle \Omega, I'J'F | H_{\text{hf,eff}} | \Omega, IJF \rangle \\ = eqQg_{eQq} + Cg_{\text{SR}} + dg_{\text{TSS}} + \delta g_{\text{SSS}} + eg_e \\ + fg_f + hg_h + hHg_{hH}, \end{aligned} \quad (3)$$

where the geometrical functions  $g$ , which depend on the usual angular-momentum quantum numbers  $I$ ,  $J$ , and  $F$ , have been derived and were tabulated in Ref. 5. One can experimentally determine the effective hyperfine param-

eters, i.e.,  $eqQ$ ,  $C$ ,  $d$ , etc., by fitting the effective Hamiltonian to the hyperfine spectrum of a rovibrational transition.

Based on Bordé's FORTRAN code, a computer program that performs the nonlinear least-squares fit was developed to extract the effective hyperfine parameters from the hyperfine spectrum. We select a rotational basis set that spans  $\Delta J = 0, \pm 2, \pm 4$  to construct the Hamiltonian matrix with vibrational and rotational constants  $E_v$ ,  $B_v$ ,  $D_v$ ,  $H_v$ ,  $L_v$ , and  $M_v$  taken from the  $\text{I}_2$  atlas.<sup>24</sup> Although two neighboring vibrational levels with different  $J$  values can have a nonvanishing Franck–Condon overlap, their large energy separation ensures that the hyperfine coupling to different vibrational levels inside the  $B$  state is negligible.

A practical issue inherent in the measurement of only the main lines (transitions with  $\Delta F = \Delta J$ ) is that the fit does not permit simultaneous determination of the respective hyperfine parameters for the  $B$  and  $X$  states. Without additional information, only the difference between the hyperfine parameters in the upper and ground levels can be reliably obtained. To separate the  $B$ -state parameters from the  $X$ -state parameters we selectively excite the transitions with low vibrational level  $v'' = 0$  [transitions  $P(49)$  59–1 and  $R(45)$  60–1 are two exceptions] and relate the  $J$  dependence of the ground-level parameters  $eqQ_X$  and  $C_X$  to that predetermined by interpolation formulas.<sup>13,25</sup> The other two major parameters for the ground state, i.e., the tensorial and scalar spin–spin parameters  $d_X$  and  $\delta_X$ , are fixed in the fit to the values 1.524 and 3.705 kHz,<sup>13</sup> respectively, which are good approximations for low-lying vibrational levels in the  $X$  ground state.<sup>13</sup>

## 4. RESULTS AND DISCUSSION

### A. $B$ -State Effective Hyperfine Parameters in the Region $42 \leq v' \leq 70$

In the wavelength range 500–517 nm we measured hyperfine spectra of 79  $B \leftarrow X$  rovibrational transitions that cover a large set of rotational and vibrational quantum numbers in the  $B$  state. These transitions were chosen to include upper vibrational levels starting at  $v' = 42, 43$  and thence progressing in increments of 2 to  $v' = 63$ : For each of these vibrational levels, we measured four to seven rotational levels that spread roughly from  $J' = 10$  to  $J' = 100$ . Above  $v' = 63$ , three vibrational levels,  $v' = 65, 69, 70$ , were accessed, and the rotational levels measured for each vibrational level are restricted to the range  $J' = 30$ –60 owing to the weak transition moment associated with this region. In addition to the above data set, six rotational levels at  $v' = 60$  and two rotational levels at  $v' = 50, 58$  were also measured. Most of the hyperfine spectra recorded have been fitted by the four-term effective Hamiltonian, and the extracted hyperfine parameters, together with the corresponding standard deviations, are listed in Table 1.

First, for the transition  $P(13)$  43–0 the four effective parameters obtained by our measurement are in good agreement with previous results within the measurement uncertainties. The standard deviation of the fit is typically 10–20 kHz for levels below  $v' = 55$  and is caused

**Table 1. B-State Effective Hyperfine Parameters Derived from the Measurement of  $^{127}\text{I}_2$  Rovibrational Transitions in the Wavelength Range 500–517 nm<sup>a</sup>**

Transition	eqQ <sub>B</sub> (MHz) <sup>b</sup>	C <sub>B</sub> (MHz) <sup>b</sup>	d <sub>B</sub> (MHz) <sup>c</sup>	δ <sub>B</sub> (MHz) <sup>c</sup>	Standard Deviation (kHz)
P(10) 42–0	–557.119(20) <sup>d</sup>	0.176138(96)	–0.08916(86)	–0.00520(85)	7.6
P(19) 42–0	–556.988(66)	0.17666(17)	–0.0921(43)	–0.0016(39)	33
R(30) 42–0	–557.184(44)	0.177751(85)	–0.0946(22)	0.0099(33)	22
R(41) 42–0	–557.553(30)	0.179178(24)	–0.0929(20)	–0.0003(16)	17
R(49) 42–0	–557.612(50)	0.180487(46)	–0.0915(25)	0.0051(23)	30
P(13) 43–0	–558.613(18)	0.190361(78)	–0.09899(62)	–0.00083(56)	10
P(25) 43–0	–558.823(15)	0.191161(39)	–0.1009(12)	0.0025(11)	9.4
R(27) 43–0	–558.667(23)	0.191593(38)	–0.0988(16)	0.0015(12)	11
P(38) 43–0	–558.565(12)	0.192839(21)	–0.10109(69)	–0.00001(81)	5.9
R(40) 43–0	–558.604(17)	0.193497(14)	–0.10303(86)	0.00034(86)	6.4
R(63) 43–0	–559.456(16)	0.198545(12)	–0.10629(90)	0.00234(85)	11
R(21) 45–0	–560.838(13)	0.223669(23)	–0.12073(80)	0.00623(57)	7.6
R(52) 45–0	–561.356(22)	0.229843(18)	–0.1239(10)	0.0095(15)	10
P(69) 45–0	–561.804(11)	0.2349204(71)	–0.12617(80)	0.00739(59)	6.8
P(91) 45–0	–562.546(13)	0.2452897(55)	–0.1324(10)	0.00975(82)	7.9
R(31) 47–0	–562.816(27)	0.264762(35)	–0.1390(16)	0.0172(12)	12
R(51) 47–0	–563.294(12)	0.270529(10)	–0.14741(84)	0.01588(64)	7.0
R(92) 47–0	–564.742(23)	0.293399(10)	–0.1598(10)	0.0200(13)	9.4
R(111) 47–0	–565.651(56)	0.310759(29)	–0.1626(44)	0.0254(35)	37
P(19) 49–0	–564.6327(72)	0.309250(21)	–0.16923(43)	0.02631(31)	4.6
P(41) 49–0	–564.886(26)	0.314896(28)	–0.1706(18)	0.0262(13)	16
P(62) 49–0	–565.295(39)	0.324667(25)	–0.1794(17)	0.0326(22)	16
R(93) 49–0	–566.485(19)	0.3509271(87)	–0.1940(13)	0.0403(10)	11
P(108) 49–0	–567.273(24)	0.3662298(84)	–0.1996(10)	0.0427(13)	9.7
R(55) 50–0	–566.0544(80)	0.3504090(55)	–0.19199(56)	0.03910(46)	4.7
R(20) 51–0	–566.275(21)	0.366031(35)	–0.20074(96)	0.0469(11)	7.1
P(30) 51–0	–566.415(29)	0.368223(40)	–0.2005(13)	0.0401(19)	13
P(50) 51–0	–566.763(14)	0.377297(11)	–0.20747(63)	0.05024(66)	5.6
P(73) 51–0	–567.132(23)	0.394644(14)	–0.2134(16)	0.0552(12)	12
P(90) 51–0	–567.872(28)	0.413339(14)	–0.2258(13)	0.0628(19)	13
R(32) 53–0	–567.752(27)	0.437830(32)	–0.2383(12)	0.0785(16)	11
R(51) 53–0	–568.171(11)	0.450037(11)	–0.24241(82)	0.08388(55)	6.6
P(70) 53–0	–568.623(34)	0.466803(19)	–0.2535(15)	0.0937(19)	14
R(89) 53–0	–569.274(40)	0.493524(21)	–0.2664(27)	0.1073(19)	21
R(21) 55–0	–568.807(18)	0.513082(32)	–0.2718(12)	0.12206(91)	10
P(61) 55–0	–569.444(22)	0.544230(21)	–0.2854(16)	0.1444(13)	15
P(83) 55–0	–570.208(27)	0.579914(17)	–0.3006(16)	0.1701(13)	15
P(102) 55–0	–571.145(42)	0.626595(27)	–0.3212(21)	0.2092(28)	22
P(19) 57–0	–569.534(27)	0.605935(82)	–0.3091(19)	0.1993(11)	15
P(33) 57–0	–569.335(44)	0.614577(46)	–0.3103(26)	0.2058(20)	23
R(65) 57–0	–571.765(86)	0.660831(90)	–0.4260(68)	0.3647(59)	60
R(74) 57–0	–570.210(94)	0.678716(54)	–0.3092(44)	0.2500(65)	44
P(80) 57–0	–570.38(12)	0.688579(74)	–0.298(14)	0.240(21)	37
R(83) 57–0	–570.632(90)	0.702332(76)	–0.311(12)	0.280(11)	46
R(95) 57–0	–570.701(83)	0.741636(48)	–0.3270(59)	0.3323(50)	51
P(17) 59–0	–568.58(15)	0.72125(42)	–0.290(13)	0.141(11)	73
P(27) 59–0	–573.49(28)	0.71536(54)	–0.569(14)	0.382(14)	131
R(28) 59–0	–573.32(48)	0.72088(55)	–0.476(24)	0.316(18)	93
P(49) 59–1	–571.695(39)	0.750322(35)	–0.4326(26)	0.3335(20)	22
R(81) 59–0	–572.12(11)	0.840592(60)	–0.4355(78)	0.4337(59)	65
P(87) 59–0	–572.555(90)	0.856503(46)	–0.4360(65)	0.4444(55)	55
P(21) 60–0	–569.937(20)	0.783323(37)	–0.3773(13)	0.34612(86)	11
R(34) 60–0	–569.964(45)	0.799015(53)	–0.3820(20)	0.3619(30)	21
R(45) 60–1	–570.446(92)	0.816760(82)	–0.3800(62)	0.3793(37)	43
R(99) 60–0	–573.28(23)	1.03267(11)	–0.499(17)	0.688(14)	121
P(17) 61–0	–569.550(24)	0.850067(59)	–0.3944(14)	0.4414(10)	13
R(36) 61–0	–569.603(42)	0.875111(89)	–0.4056(19)	0.4638(27)	16

(Table Continued)

**Table 1. Continued**

Transition	$eqQ_B$ (MHz) <sup>b</sup>	$C_B$ (MHz) <sup>b</sup>	$d_B$ (MHz) <sup>c</sup>	$\delta_B$ (MHz) <sup>c</sup>	Standard Deviation (kHz)
<i>P</i> (53) 61–0	−570.037(79)	0.906087(75)	−0.4162(42)	0.5154(42)	44
<i>P</i> (83) 61–0	−570.14(14)	1.02283(10)	−0.422(10)	0.6224(83)	87
<i>P</i> (23) 63–0	−568.464(78)	1.01785(15)	−0.4219(56)	0.6974(44)	46
<i>R</i> (31) 63–0	−568.62(11)	1.03395(15)	−0.4281(76)	0.7225(58)	70
<i>P</i> (43) 63–0	−568.854(83)	1.05691(12)	−0.4436(43)	0.7560(36)	40
<i>P</i> (52) 63–0	−569.08(11)	1.084930(90)	−0.4532(49)	0.7987(73)	51
<i>P</i> (19) 65–0	−566.342(63)	1.21056(14)	−0.4648(37)	1.0373(32)	43
<i>P</i> (33) 65–0	−566.504(73)	1.24010(14)	−0.4893(33)	1.0966(34)	46
<i>R</i> (43) 65–0	−567.21(11)	1.28195(20)	−0.4901(68)	1.1712(49)	57
<i>P</i> (33) 69–0	−558.63(12)	1.85049(22)	−0.6800(72)	2.3114(69)	44
<i>P</i> (39) 69–0	−560.05(23)	1.89425(41)	−0.696(12)	2.422(10)	119
<i>R</i> (44) 69–0	−561.17(27)	1.96255(38)	−0.732(12)	2.5258(96)	76
<i>R</i> (49) 69–0	−559.39(26)	2.02075(33)	−0.854(14)	2.559(14)	116
<i>P</i> (53) 69–0	−562.09(50)	2.04973(57)	−0.793(28)	2.691(22)	252
<i>P</i> (35) 70–0	−557.32(24)	2.08735(37)	−0.809(12)	2.8335(88)	111
<i>R</i> (37) 70–0	−557.47(35)	2.12619(51)	−0.867(22)	2.886(14)	173
<i>R</i> (45) 70–0	−558.80(44)	2.22994(62)	−0.937(24)	3.045(17)	196

<sup>a</sup>A four-term effective Hamiltonian is used in the fit. Transitions *P*(69) 58–0, *R*(18) 59–0, *P*(84) 60–0, *P*(77) 60–0, and *P*(63) 70–0 are not included in this table because their upper-level hyperfine spectra are altered considerably by the hyperfine perturbation from a  $1_g(^1\Pi_g)$  state.

<sup>b</sup> $eqQ_X$  and  $C_X$  are determined by Eqs. (14) and (10), respectively, of Ref. 13 and are held fixed in the fit.

<sup>c</sup> $d_X$  and  $\delta_X$  are fixed in the fit to 1.524 and 3.705 kHz,<sup>13</sup> respectively.

<sup>d</sup>Quoted uncertainties ( $1\sigma$ ) are estimated from the standard deviations of the fits.

primarily by various experimental sources such as background interference fringes superimposed upon the saturation resonance, residual cavity drift, variations of the optical power and alignment arising from the frequency scan, and residual amplitude modulation in the saturated-absorption spectroscopy.

At rovibrational levels above  $v' = 55$ , transitions *R*(65) and *R*(74) of the 57–0 band and *P*(17), *P*(27), and *R*(28) of the 59–0 band distinguish themselves from adjacent transitions by large standard deviations that cannot be explained by the experimental sources mentioned above. Furthermore, fits for transitions *P*(69) 58–0, *R*(18) 59–0, *P*(77) 60–0, and *P*(63) 70–0 produce very large standard deviations (0.3–1 MHz), and the hyperfine spectrum of the *P*(84) 60–0 transition cannot be fitted at all by the effective hyperfine Hamiltonian. We attribute this abnormality to the influence of the same  $1_g(^1\Pi_g)$  state that strongly perturbs the  $v' = 76, 77, 78$  vibrational levels close to the dissociation limit. Because of the strong perturbation, hyperfine spectra at these transitions cannot be fully described by the effective Hamiltonian based on the second-order perturbation; hence these transitions are not included in Table 1. The source of this perturbation is confirmed and its specific properties in the intermediate region that we investigate are discussed further in Subsection 4.C.

We have also attempted to introduce the last four terms in Eq. (3). At levels of  $v' = 57–65$ , these four additional terms do not improve the standard deviations of the fits. Besides, effective parameters  $e, f, g$ , and  $hH$  derived from the new fits all have large uncertainties that are comparable to the fitted values, and contradict the smooth trend of the second-order contribution by altering their signs across adjacent rotational levels. Although vibrational levels with  $v' > 65$  would be better candidates for testing these additional terms because of the increasing pertur-

bation, the present large uncertainties associated with these weak transitions preclude any accurate assessment. Also, as pointed out in Ref. 5, the total number of hyperfine parameters that can be fitted reliably is restricted by the use of a maximum of 15 or 21 main lines in the hyperfine spectrum.

## B. Rovibrational Dependence of Hyperfine Parameters As a Result of the Second-Order Effect

Four hyperfine parameters,  $eqQ_B$ ,  $C_B$ ,  $d_B$ , and  $\delta_B$ , all exhibit systematic rovibrational dependence in the measured vibrational levels from  $v' = 42$  to  $v' = 70$ . Figures 2–4 display variations of these parameters. In the figures each solid line is a fit of experimental data for  $J$  dependence that belongs to a single vibrational level  $v'$  ( $v'$  is indicated as a number attached to each line in the figures). In general, these parameters have monotonic dependence on both rotational and vibrational quantum numbers, except for the levels in the vicinity of  $v' = 57–59$ , where strong perturbation from the  $1_g(^1\Pi_g)$  state produces irregularities that superpose upon the smooth second-order background.

Except for the variation of  $eqQ_B$  at vibrational levels lower than  $v' = 60$ , the smooth and monotonic trend of these effective hyperfine parameters is well characterized by the second-order perturbation. For instance, spin-rotation parameter  $C_B$  can be expressed as<sup>4,5,11,27</sup>

$$C_B(v, J) = C_D(v, J) - \sum_{\Omega'} \left[ \sum_{v'} \frac{\langle V^0 \rangle \langle V^1 \rangle}{E_{0_u^+ v' J} - E_{\Omega' v' J}} + \int \frac{\langle V^0 \rangle \langle V^1 \rangle}{E_{0_u^+ v' J} - E_{\Omega' J}} \rho(E_{\Omega' J}) dE_{\Omega' J} \right]. \quad (4)$$

First-order contribution  $C_D$  is less than 0.15 kHz,<sup>5</sup> which is negligible compared with the second-order contribution. The summation and integration in brackets in Eq.

(4) together account for the second-order contribution from both discrete levels ( $v', J$ ) and energy continuum  $E_J$  inside each perturbing electronic state  $\Omega'$ . In the numerators  $\langle V^0 \rangle$  and  $\langle V^1 \rangle$  denote gyroscopic and magnetic

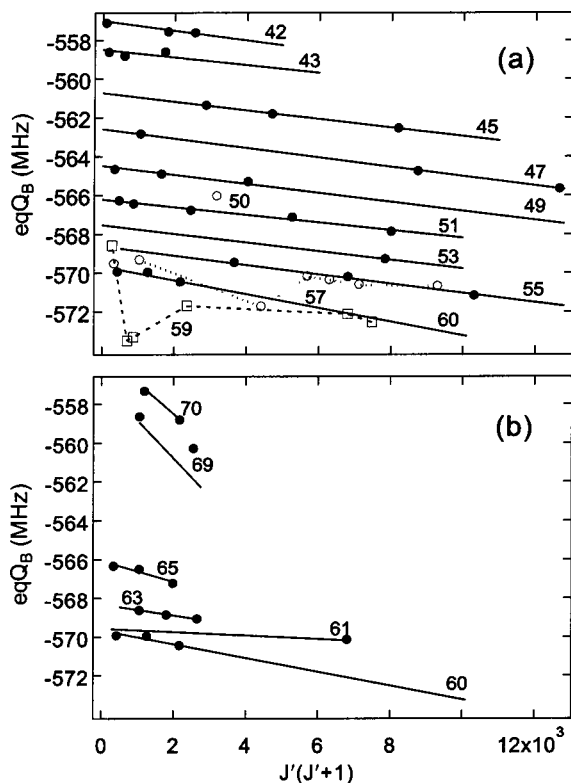


Fig. 2. Rovibrational dependence of  $eqQ_B$ . Each solid line is the linear fit in  $J'(J'+1)$  of experimental data that belong to one vibrational level,  $v'$  ( $v'$  is indicated as a number attached to each line). Experimental data (squares and open circles) show abnormal variations near  $v' = 57, 59$ . The vibrational dependence of  $eqQ_B$  reverses its trend after  $v' = 60$  and overlaps that of lower  $v'$  levels. Also, in the region  $v' = 57-60$  several rovibrational levels experience strong perturbation from the  $1_g(^1\Pi_g)$  state; thus  $eqQ_B$  for these levels are not shown in the figure.

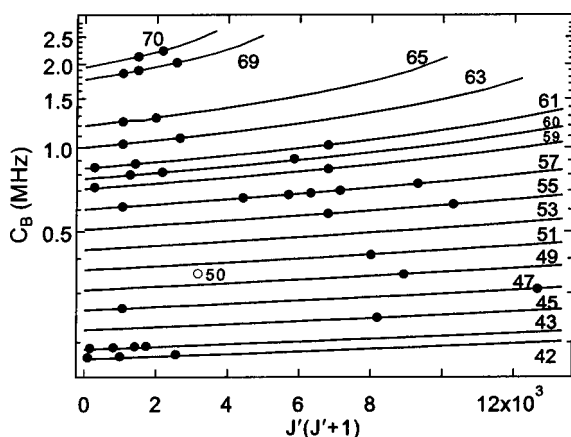


Fig. 3. Semilog plot of rovibrational dependence of  $C_B$ . Each solid line, calculated from interpolation function  $C_B(R)$  [see Fig. 7(b) below], is the  $J$  dependence for one vibrational level  $v'$  ( $v'$  is indicated as a number attached to each line). Unlike  $eqQ_B$ ,  $d_B$ , and  $\delta_B$ ,  $C_B$  does not have abnormal variations near  $v' = 57, 59$  because the gyroscopic Hamiltonian, which is involved only in  $C_B$ , cannot couple the  $B$  and  $1_g(^1\Pi_g)$  states.

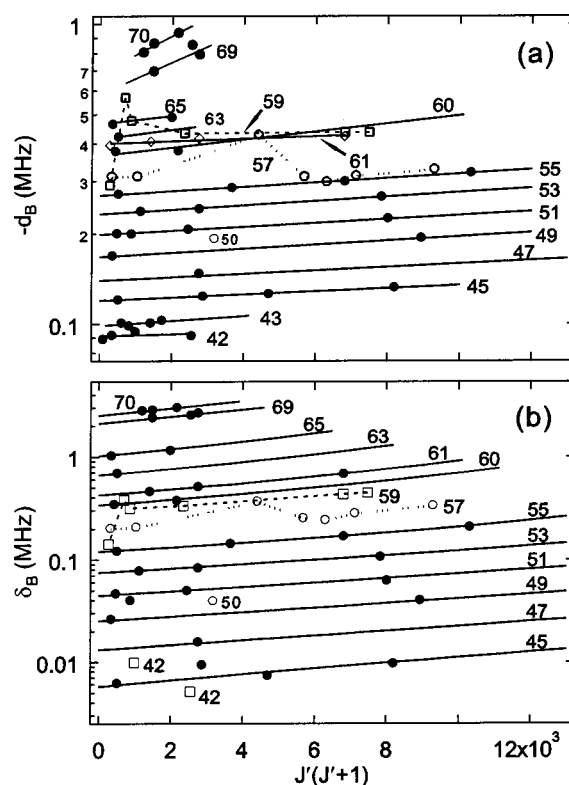


Fig. 4. Semilog plot of rovibrational dependence of  $d_B$  and  $\delta_B$ . Note that the vertical scale has been inverted for  $d_B$ . Each solid line is the linear fit in  $J'(J'+1)$  of experimental data that belong to one vibrational level,  $v'$  ( $v'$  is indicated as a number attached to each line). Experimental data (squares and open circles) show abnormal variations near  $v' = 57, 59$ . In the region  $v' = 57-60$  several rovibrational levels experience strong perturbation from the  $1_g(^1\Pi_g)$  state; thus hyperfine parameters for these levels are not shown in the figure.

dipole couplings, respectively, which can be approximated as a product of a Franck–Condon integral and a reduced electronic matrix element with the assumption that the latter has a weak  $R$  dependence.<sup>5</sup> The other three effective parameters can be expressed in the same manner with different types of hyperfine coupling.<sup>4,5</sup>

As the  $B$  state rovibrational levels ( $v, J$ ) progress toward the dissociation limit, their overall Franck–Condon overlaps with the perturbing levels continue to increase while the corresponding energy denominators decrease, thereby creating monotonic trends in hyperfine parameters, with large slopes near the dissociation limit. More specifically, in a given vibrational level  $v$ , as the rotational quantum number  $J$  increases the total number of discrete vibrational levels inside each perturbing electronic state drops, whereas the contribution from energy continuum increases, so the net effect is a smooth variation of the hyperfine parameters even for large  $J$  values.

The systematic data from this study and from the literature offer a means for a complementary approach to analyzing the electronic structure of the states converging to the second dissociation limit,  $^2P_{3/2} + ^2P_{1/2}$ . Previous calculations<sup>4,11,27</sup> of hyperfine parameters can be extended to low vibrational levels as well as to the rotational dependence at each vibrational level, using the

available information on the electronic wave functions and the related potential energy curves (PEC) determined either by experiment<sup>28,29</sup> or by theoretical calculation.<sup>8</sup> Several interesting issues can be addressed with the help of these calculations, such as (1) to what extent the separated-atom wave functions can be extrapolated to short internuclear separations, (2) an estimation of the admixture between those related components in the separated-atom basis set, and (3) how sensitively the hyperfine parameters depend on the choice of PECs.

### C. Perturbation from the $1_g(^1\Pi_g)$ State

Apart from second-order effect, we observed strong perturbation in the intermediate region that spans  $v' = 42\text{--}70$ . Hyperfine parameters  $eqQ_B$ ,  $d_B$ , and  $\delta_B$  all exhibit abnormal  $J$  dependence for levels  $v' = 57, 59$ , which are clearly shown in Figs. 2 and 4. Moreover, as we pointed out in Subsection 4.A, hyperfine spectra of several transitions have exceptionally large residual errors in the fit or cannot be fitted by the effective hyperfine Hamiltonian in the region  $v' = 57\text{--}60$ .

The nature of this perturbation is analogous to that of the rotational and vibrational perturbations studied in a variety of molecules. Among the cluster of electronic states converging with the  $B$  state, the  $1_g(^1\Pi_g)$  state has a potential whose outer limb is closest to that of the  $B$  state. Thus it is possible that an approximate energy coincidence and a moderate Franck–Condon overlap between the  $B$  and the  $1_g(^1\Pi_g)$  rovibrational levels arise simultaneously as two sets of rovibrational levels progress respectively inside the  $B$  and the  $1_g(^1\Pi_g)$  states. This

perturbation depends sensitively on the energy differences among the levels involved and hence cannot be treated by the effective Hamiltonian based on the second-order perturbation.

The strong  $u\text{--}g$  mixing that we recorded at transition  $P(84) 60\text{--}0$  permits a more quantitative analysis. The hyperfine spectrum of this transition is shown in Fig. 5, where vertical bars labeled  $a_1\text{--}a_{15}$  above the spectrum are simulated by the four-term effective Hamiltonian with the hyperfine parameters obtained by interpolation of the parameters of neighboring rovibrational levels. This simulation produces the spectrum in the absence of strong perturbation. As shown in Fig. 5, the  $a_{10}$  component does not show up at the position predicted by the simulation; instead, at least four new components, namely,  $b_1\text{--}b_4$ , emerge nearby: Apparently the  $a_{10}$  upper level is strongly perturbed by hyperfine levels of a perturbing electronic state and the mixed levels appear as  $b_1$  and  $b_3$ , with the crossover  $b_2$  sitting in the middle.

The  $a_{10}$  upper level ( $F = 87$ ,  $J = 83$ , and  $I = 4$ ) is isolated from other hyperfine levels inside the  $B$  state because it is coupled to only two hyperfine levels with large energy separations ( $\sim 111$  GHz). However, such is not necessarily true for the perturbing electronic state: Calculation that uses the  $B$  and  $1_g(^1\Pi_g)$  empirical PECs<sup>28,29</sup> shows that the perturbing levels could be the two hyperfine levels (resulting from linear combinations of  $I' = 3, 5$ ) at rovibrational level ( $v' = 15$ ,  $J' = 84$ ) inside the  $1_g(^1\Pi_g)$  state. Nevertheless, judging from the relatively large strength of the  $b_1$  and  $b_3$  components, an effective two-level model, characterized by a energy differ-

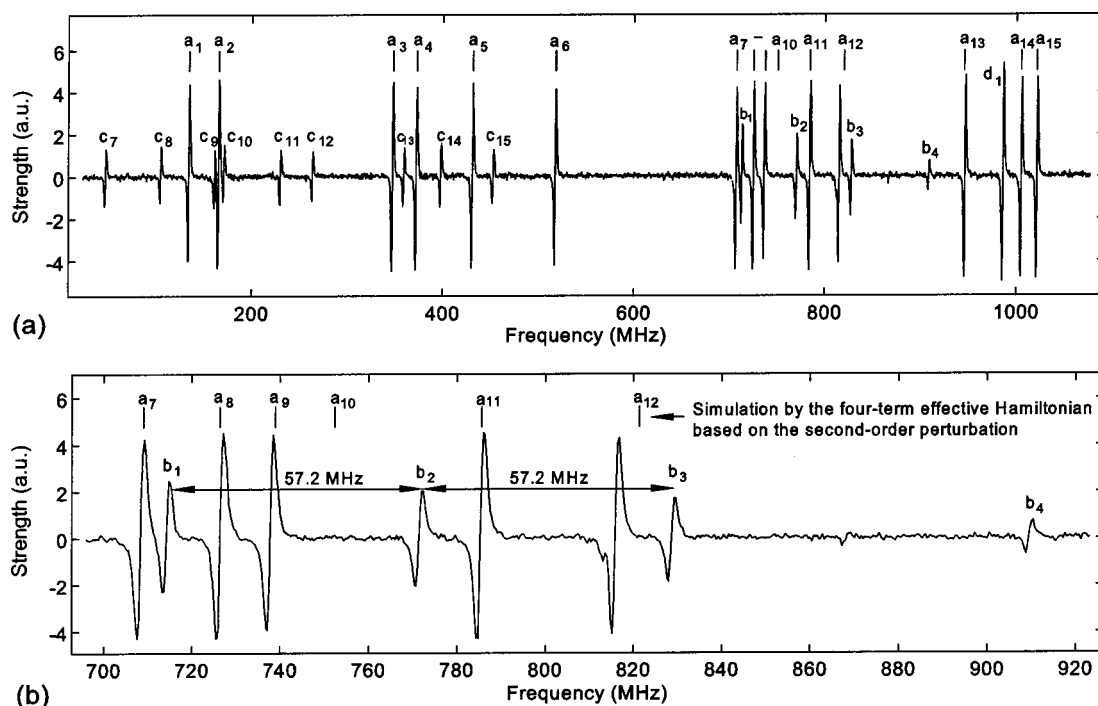


Fig. 5. Strong  $u\text{--}g$  perturbation observed at transition  $P(84) 60\text{--}0$ . (a) The whole spectrum; the part of interest (700–920 MHz) is expanded and replotted in (b), where  $b_1\text{--}b_4$  arise from  $u\text{--}g$  mixing between the  $B$  and the  $1_g(^1\Pi_g)$  states and  $b_2$  is the crossover of  $b_1$  and  $b_3$ . In (a)  $c_7\text{--}c_{15}$  are identified as lines of a neighboring transition  $R(30) 64\text{--}1$ , and  $d_1$ , left of  $a_{14}$ , belongs to another transition,  $P(81) 59\text{--}0$ . The vertical bars labeled  $a_1\text{--}a_{15}$  indicate roughly the hyperfine spectrum that the  $P(84) 60\text{--}0$  transition would assume if there were no such strong perturbation from the  $1_g(^1\Pi_g)$  state. Note that the  $1_g(^1\Pi_g)$  state is also designated  $1'_g$  or  $c1_g$  in the literature.

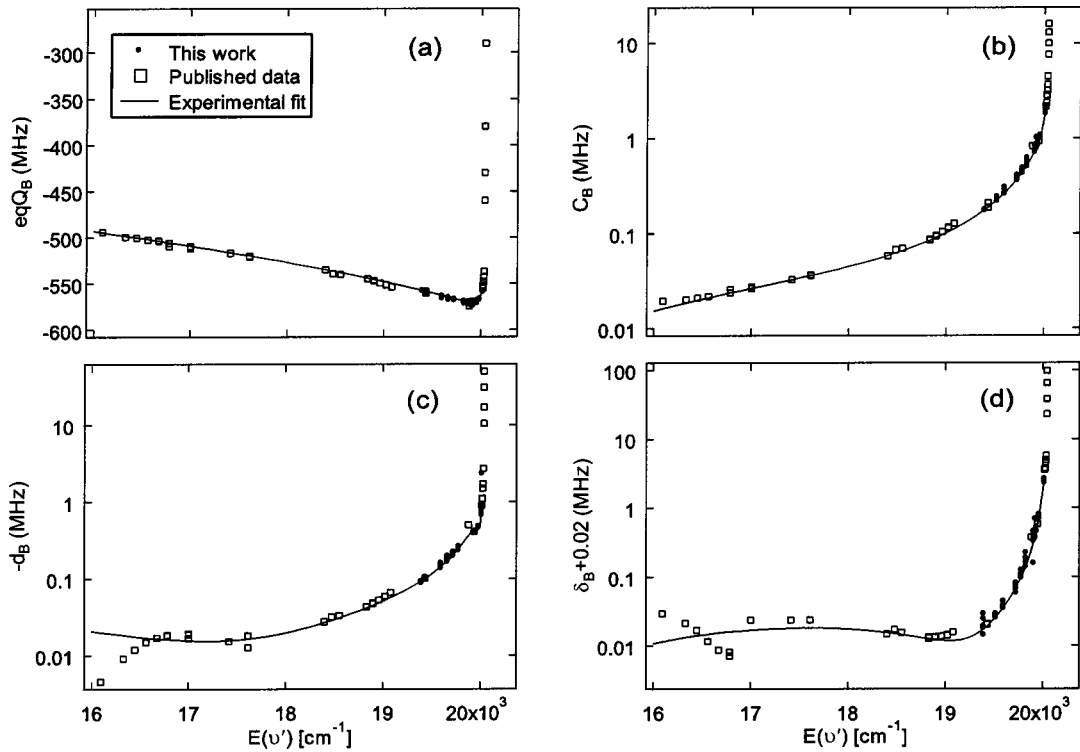


Fig. 6. Vibrational dependence of the  $B$ -state hyperfine parameters  $eqQ_B$ ,  $C_B$ ,  $d_B$ , and  $\delta_B$ . Note that a semilog plot is used for  $C_B$ ,  $d_B$ , and  $\delta_B$ . The steep trend near the dissociation energy is due to the perturbations from the electronic states converging with the  $B$  state to the second dissociation limit:  ${}^2P_{3/2} + {}^2P_{1/2}$ . See text for details.

ence  $\Delta E$  and an interacting matrix element  $H_{12}$ , is adequate for estimating the hyperfine-coupling strength between the  $B$  and the  $1_g({}^1\Pi_g)$  states. Accordingly, the two mixed states can be written as

$$\begin{aligned} |1\rangle &= \alpha|B, vJIF\rangle + \beta|1_g, v'J'\epsilon'F\rangle, \\ |2\rangle &= -\beta|B, vJIF\rangle + \alpha|1_g, v'J'\epsilon'F\rangle, \end{aligned} \quad (5)$$

where  $\epsilon'$  labels the nuclear spin wave function of the perturbing level. Simple calculation that uses the frequency differences among  $b_1$ ,  $b_3$ , and simulated  $a_{10}$  gives the energy difference  $\Delta E = 39$  MHz, hyperfine coupling  $H_{12} = 54$  MHz, and mixing parameters  $\alpha = 0.82$  and  $\beta = 0.57$ . With the same PECs of the  $B$  and  $1_g({}^1\Pi_g)$  states we calculated the Franck-Condon overlap  $|\langle v'|v\rangle|$  to be 0.1 and then estimated the electronic matrix element for the hyperfine coupling as  $|\langle B0_u^+|H_{\text{hf}}|1_g({}^1\Pi_g)\rangle| = 540$  MHz.

Electronic states other than the  $1_g({}^1\Pi_g)$  state are unlikely to produce such strong perturbation because the associated Franck-Condon overlaps for levels at which the energy coincidence could happen are at least 2 orders of magnitude smaller. Even if the perturbation from such a state can shift a particular hyperfine level on the kilohertz level, it cannot produce a noticeable influence on the whole hyperfine structure at a certain rovibrational level in this intermediate region because the strict energy equality needed can be satisfied only for a small number of hyperfine levels.

In this intermediate region, owing to the relatively large differences in the vibrational and rotational constants and the moderate Franck-Condon overlap between the  $1_g({}^1\Pi_g)$  and the  $B$  states, these resonances

each span only a small range of rotational levels, a property that is clearly identified in Figs. 2 and 4. These abnormal variations directly confirm the previously observed  $u-g$  mixing between the  $1_g({}^1\Pi_g)$  and the  $B$  states at rotational levels centered on  $J' = 22$  at  $v' = 59$  through the optical-optical double-resonance experiment in which the high-lying ion-pair states with  $u$  symmetry were accessed.<sup>29</sup>

#### D. Vibrational Dependence of Hyperfine Parameters in the $B$ State

Combining the data from the study reported here and from the literature<sup>4,13,15,25,30-39</sup> has facilitated investigations of the hyperfine spectra that now cover a majority of the vibrational levels ( $3 \leq v' \leq 82$ ) in the  $B$  state. Therefore it is now possible to explore the global trend of these hyperfine parameters in the  $B$  state and uncover useful systematic variations of these hyperfine interactions.

With the rotational dependence being suppressed, the hyperfine parameters as functions of pure vibrational energy  $E(v')$  are illustrated in Fig. 6. As shown in the figure, the values of these hyperfine parameters increase rapidly when the molecule approaches the dissociation limit, which, as discussed in Subsection 4.B, is a result of the perturbations from the cluster of electronic states that share the same dissociation limit with the  $B$  state. Whereas the variation in values of  $C_B$  is essentially smooth over the whole range of vibrational energies,  $eqQ_B$ ,  $d_B$ , and  $\delta_B$  all have local irregularities at several regions. First, in the region  $3 \leq v' \leq 17$  [ $16\,000 \text{ cm}^{-1} \leq E(v') \leq 17\,700 \text{ cm}^{-1}$ ], both  $d_B$  and  $\delta_B$  have visible fluctuations because of the magnetic dipole coupling be-

tween the  $B$  and the  $B''1_u(^1\Pi_u)$  states that arises from a potential crossover near level  $v' = 5$ .<sup>2</sup> Meanwhile, the absence of such fluctuation in  $C_B$  at these levels is due to the fact that the accompanying gyroscopic coupling, which is involved only in  $C_B$ , is a weak effect compared with the magnetic-dipole coupling.<sup>1,2,13,40,41</sup> Second, irregularities in hyperfine parameters are found for levels near  $v' = 57\text{--}60$  [ $19\,863\text{ cm}^{-1} \leq E(v') \leq 19\,915\text{ cm}^{-1}$ ] at which  $eqQ_B$ ,  $d_B$ , and  $\delta_B$  deviate from the smooth trend for a small range of rotational levels in a certain vibrational level. As discussed in Subsection 4.C, this resonancelike feature results from the hyperfine coupling between the  $B$  and  $1_g(^1\Pi_g)$  states through the rotational coincidence. Finally, the same  $1_g(^1\Pi_g)$  state strongly perturbs levels from  $v' = 76$  to  $v' = 78$  [ $E(v') \approx 20\,034\text{ cm}^{-1}$ ] with the favorable Franck–Condon overlaps and the small energy separations.<sup>4,14</sup> In last two perturbing regions,  $C_B$  also keeps its smooth trend because the gyroscopic Hamiltonian cannot couple the  $B$  state with the  $1_g(^1\Pi_g)$  state.<sup>5</sup>

The  $v$  dependence of  $eqQ_B$  reverses its trend after  $v' = 60$  [ $E(v') \approx 19\,915\text{ cm}^{-1}$ ]; hence its values for higher  $v'$  levels overlap those of lower  $v'$  levels, a consequence of the two effects that dominate at different regions: a first-order term—the interaction between nuclear quadrupole moment  $Q$  and electric field gradient  $q$ —increases with decreasing vibrational energy but approaches a constant value at large energies at which the second-order term from perturbing electronic states moves in gradually and causes a steep trend near the dissociation energy.

## E. Radial Dependence of the Hyperfine Interaction

In this subsection we examine the variation of the hyperfine interaction with internuclear separation  $R$ . Because hyperfine parameters already involve averaging over the molecular rotation, the electronic motion in the molecular frame, and the nuclear vibration, it is also desirable to remove the last vibrational average in these parameters such that a straightforward relation between the hyperfine interaction and the internuclear separation can be obtained.

We remove the vibrational average in the hyperfine parameters by inverting the expression  $O(v', J') = \langle v'_{J'} | O(R) | v'_{J'} \rangle$ , where  $O(v', J')$  denotes one of the four hyperfine parameters for a particular level ( $v', J'$ ) in the  $B$  state and  $|v'_{J'}\rangle$  is the corresponding vibrational wave function (properly normalized). The inversion is made by expansion of the function  $O(R)$  as a polynomial with its coefficients determined from an experimental fit.<sup>42,43</sup> Le Roy's program LEVEL<sup>44</sup> is used in the inversion process to calculate the vibrational wave functions from the  $B$ -state potential energy curve.<sup>28</sup> Figure 7 plots  $eqQ(R)$ ,  $C_B(R)$ ,  $d_B(R)$ , and  $\delta_B(R)$ , along with the corresponding residual errors of the interpolation. Consistent with the smooth variation in  $C_B$ , interpolation function  $C_B(R)$  has small residual errors (within  $\pm 0.02$ , relative) for the entire range  $v' = 3\text{--}70$ , as shown in the inset of Fig. 7(b). Conversely, the large residual errors in the interpolation of  $eqQ_B$ ,  $d_B$ , and  $\delta_B$  for  $v' \geq 56$  reflect

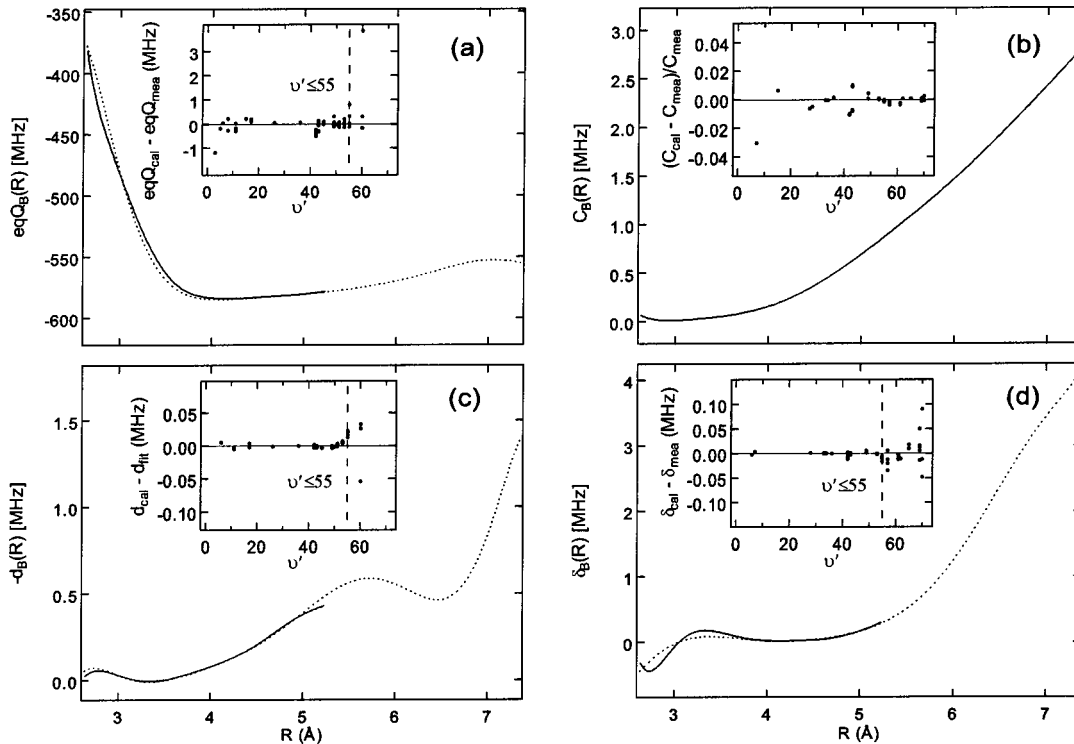


Fig. 7.  $R$  dependence of hyperfine operators  $eqQ_B(R)$ ,  $C_B(R)$ ,  $d_B(R)$ , and  $\delta_B(R)$ . These hyperfine operators are obtained by inversion of the expression  $O_{v',J'} = \langle v'_{J'} | O(R) | v'_{J'} \rangle$ , where  $O$  represents one of the hyperfine parameters. Insets are residual errors of the interpolation. (a), (c), (d) Solid and dashed curves are fits up to  $v' = 55$  and  $v' = 70$ , respectively. The fit in (b) is up to  $v' = 70$ . The large residual errors for  $eqQ_B$ ,  $d_B$ , and  $\delta_B$  in the region  $55 < v' \leq 70$  are due to strong perturbation from the  $1_g(^1\Pi_g)$  state.

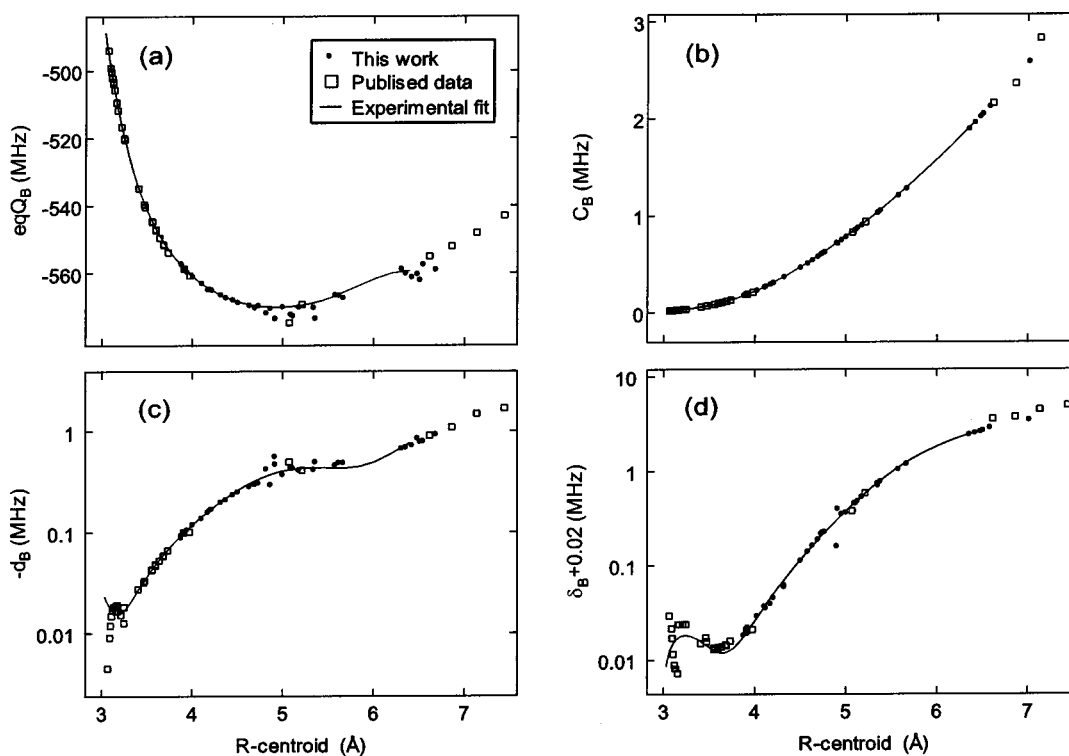


Fig. 8.  $eqQ_B$ ,  $C_B$ ,  $d_B$ , and  $\delta_B$  versus  $R$  centroid ( $\langle v'_{J'} | R | v'_{J'} \rangle$ ). Solid curves were calculated from the interpolation functions for these hyperfine parameters. The data presented here cover a relatively large range of internuclear separation and join the previous results at both small and large internuclear separations. The visible scatter of the data points in  $eqQ_B$ ,  $d_B$ , and  $\delta_B$  near 5 Å is due to the strong perturbation from the  $1_g(^1\Pi_g)$  state.

their abnormal variations observed near  $v' = 57, 59$  [see the insets in Fig. 7], restricting a reliable interpolation only to levels of  $v' < 56$ .

The hyperfine parameters extracted from the spectra are directly associated with specific quantum numbers ( $v', J'$ ) but not internuclear separation  $R$ . Alternatively, these hyperfine parameters can be plotted against  $R$  centroid ( $\langle v'_{J'} | R | v'_{J'} \rangle$ ), which is the expectation value of the internuclear separations sampled by the nuclear vibration and evaluated by use of the same  $B$ -state potential.<sup>28</sup> Figure 8 shows such plots for  $eqQ_B$ ,  $C_B$ ,  $d_B$ , and  $\delta_B$ , where solid curves are calculated from  $\langle v'_{J'} | O(R) | v'_{J'} \rangle$  and symbols are experimental data. Again, the visible scatter of data points in  $eqQ_B$ ,  $d_B$ , and  $\delta_B$  near 5 Å (=0.5 nm) is due to the strong perturbation from the  $1_g(^1\Pi_g)$  state.

In the region  $R < 5$  Å, valuable information can readily be extracted from  $eqQ_B$  to assist the investigation of the electronic structure of  $^{127}\text{I}_2$ . Unlike the other three hyperfine parameters whose major parts originate from perturbations at nearly all possible values of  $R$ , a significant part of  $eqQ_B$  is due to the interaction between nuclear quadrupole moment  $Q$  and electric field gradient  $q(R)$  generated by the surrounding charge distribution of a largely  $B$ -state character.<sup>5,45</sup> This fact is more evident if we focus on the region  $R < 5$  Å, where perturbations from other electronic states are negligible by comparison. Moreover, when they move from a separated-atom model to small internuclear separation, the two atomic wave functions are increasingly distorted, their overlapping also increases, and hence  $eqQ_B$  deviates gradually from

Table 2. Vibration-Removed Interpolation Function  $eqQ_B(R)$ <sup>a</sup>

$i$	$\alpha_i$
0	-487.80(17) <sup>b</sup>
1	-236(11)
2	112(26)
3	163(28)
4	-210(18)
5	87.8(6.5)
6	-12.73(94)
Standard deviation (MHz)	
	0.21

<sup>a</sup> $eqQ_B(R) = \sum_{i=0}^6 \alpha_i (R - R_e)^i$ ,  $3 \text{ \AA} < R < 5 \text{ \AA}$ , and  $R_e = 3.027082$  Å. The fit includes 69 levels with  $v' < 57$ , which are taken from this study and from published data summarized in Refs. 13 and 25.

<sup>b</sup>Quoted uncertainties ( $1\sigma$ ) are estimated from the standard deviations of the fit.

the value calculated from a separated-atom basis set or linear combinations of atomic orbitals. Therefore, when  $R < 5$  Å, the vibration-removed interpolation function  $eqQ_B(R)$ , coupled with *a priori* information on  $q(R)$ , can be used to determine iodine's nuclear quadrupole moment or to serve as a benchmark for molecular *ab initio* calculations of the electronic structure at various values of  $R$ . For this purpose we list in Table 2 the coefficients of the interpolation function for  $eqQ_B(R)$  over the range  $R = 3\text{--}5$  Å.

## 5. CONCLUSIONS

Hyperfine interactions in the  $B0_u^+(^3\Pi_u)$  state of  $^{127}\text{I}_2$  have been systematically studied. By saturated-absorption

spectroscopy of hyperfine spectra of the  $B \leftarrow X$  transitions at a wavelength range 500–517 nm, four effective hyperfine parameters,  $eQqQ_B$ ,  $C_B$ ,  $d_B$ , and  $\delta_B$ , were determined for a large number of rovibrational levels spanning the intermediate region ( $42 \leq v' \leq 70$ ), yielding rich information about the rotational and vibrational dependence of the hyperfine parameters. In addition to the second-order effect that is responsible for the smooth trend of these hyperfine parameters, abnormal variations in  $eQqQ_B$ ,  $d_B$ , and  $\delta_B$  at vibrational levels  $v' = 57$ –60 have been observed, and it was found that some hyperfine spectra in this region cannot be fully described by the effective hyperfine Hamiltonian. By examining the cluster of electronic states converging with the  $B$  state and the strong  $u$ – $g$  mixing recorded at transition  $P(84) 60$ –0, we have concluded that these anomalies are caused by the hyperfine perturbation from the  $1_g(^1\Pi_g)$  electronic state through the rotational coincidence, which confirms the previous observation of  $u$ – $g$  mixing at level  $v' = 59$  in the optical–optical double-resonance excitation of the ion-pair states with  $u$  symmetry. Various perturbation effects in the  $B$  state so far identified have been summarized briefly. We also examined the radial dependence of the hyperfine interactions by removing the vibrational average in the hyperfine parameters.

The systematic determination of hyperfine parameters in the intermediate region provides useful information for applications of optical frequency stabilization that explore the transitions with wavelengths below 517 nm. Also, extension of the calculation of the hyperfine parameters to low-lying vibrational levels as well as to their rotational dependence permits a detailed analysis of the molecular electronic structure from the perspective of hyperfine interactions.

## ACKNOWLEDGMENTS

We thank J. L. Hall for his interest in this study. This research is financially supported by NASA, the National Science Foundation, the U.S. Office of Naval Research, and the National Institute of Standards and Technology.

J. Ye's e-mail address is ye@jila.colorado.edu.

\*Permanent address, Department of Physics, National Dong Hwa University, Hualien 974, Taiwan.

## REFERENCES

- J. Vigué, M. Broyer, and J. C. Lehmann, "Natural hyperfine and magnetic predissociation of the  $I_2 B$  state. I. Theory," *J. Phys. (Paris)* **42**, 937–947 (1981).
- J. Vigué, M. Broyer, and J. C. Lehmann, "Natural hyperfine and magnetic predissociation of the  $I_2 B$  state. II. Experiments on natural and hyperfine predissociation," *J. Phys. (Paris)* **42**, 949–959 (1981).
- J. P. Pique, F. Hartmann, S. Churassy, and R. Bacis, "Hyperfine interactions in homonuclear diatomic molecules and  $u$ – $g$  perturbations. I. Theory," *J. Phys. (Paris)* **47**, 1909–1916 (1986).
- J. P. Pique, F. Hartmann, S. Churassy, and R. Bacis, "Hyperfine interactions in homonuclear diatomic molecules and  $u$ – $g$  perturbations. II. Experiments on  $I_2$ ," *J. Phys. (Paris)* **47**, 1917–1929 (1986).
- M. Broyer, J. Vigué, and J. C. Lehmann, "Effective hyperfine hamiltonian in homonuclear diatomic molecules. Application to the  $B$  state of molecular iodine," *J. Phys. (Paris)* **39**, 591–609 (1978).
- M. Saute and M. Aubert-Frécon, "Calculated long-range potential-energy curves for the 23 molecular states of  $I_2$ ," *J. Chem. Phys.* **77**, 5639–5646 (1982).
- C. Teichteil and M. Pelissier, "Relativistic calculations of excited states of molecular iodine," *Chem. Phys.* **180**, 1–18 (1994).
- W. A. de Jong, L. Visscher, and W. C. Nieuwpoort, "Relativistic and correlated calculations on the ground, excited, and ionized states of iodine," *J. Chem. Phys.* **107**, 9046–9058 (1997).
- N. F. Ramsey and E. M. Purcell, "Interactions between nuclear spins in molecules," *Phys. Rev.* **85**, 143L–144L (1952).
- M. D. Levenson and A. L. Schawlow, "Hyperfine interactions in molecular iodine," *Phys. Rev. A* **6**, 10–20 (1972).
- J. Vigué, M. Broyer, and J. C. Lehmann, "Ab initio calculation of hyperfine and magnetic parameters in the  $I_2 B$  state," *Phys. Rev. Lett.* **42**, 883–887 (1979).
- A. Morinaga, "Hyperfine structure and hyperfine coupling constant of molecular iodine," *Jpn. J. Appl. Phys.* **23**, 774–775 (1984).
- B. Bodermann, H. Knöckel, and E. Tiemann, "Widely usable interpolation formulae for hyperfine splittings in the  $^{127}I_2$  spectrum," *Eur. Phys. D* **19**, 31–44 (2002).
- J. P. Pique, F. Hartmann, R. Bacis, S. Churassy, and J. B. Koffend, "Hyperfine-induced ungerade–gerade symmetry breaking in a homonuclear diatomic molecule near a dissociation limit:  $^{127}I_2$  at the  $^2P_{3/2}$ – $^2P_{1/2}$  limit," *Phys. Rev. Lett.* **52**, 267–270 (1984).
- C. J. Bordé, G. Camy, B. Decomps, and J.-P. Descoubes, "High precision saturation spectroscopy of  $^{127}I_2$  with argon lasers at 5 145 Å and 5 017 Å: main resonances," *J. Phys. (Paris)* **42**, 1393–1411 (1981).
- J. P. Pique, F. Hartmann, R. Bacis, and S. Churassy, "Hyperfine structure of higher rovibrational levels in the iodine  $B$  state studied by  $Ar^+$  laser induced fluorescence," *Opt. Commun.* **36**, 354–358 (1981).
- H. J. Foth and F. Spieweck, "Hyperfine structure of the  $R(98)$ , 58–1 line of  $^{127}I_2$  at 514.5 nm," *Chem. Phys. Lett.* **65**, 347–352 (1979).
- J. Ye, L. Robertsson, S. Picard, L.-S. Ma, and J. L. Hall, "Absolute frequency atlas of molecular  $I_2$  lines at 532 nm," *IEEE Trans. Instrum. Meas.* **48**, 544–549 (1999).
- W.-Y. Cheng, L. S. Chen, T. H. Yoon, J. L. Hall, and J. Ye, "Sub-Doppler molecular-iodine transitions near the dissociation limit (523–498 nm)," *Opt. Lett.* **27**, 571–573 (2002).
- W.-Y. Cheng, L. S. Chen, T. H. Yoon, J. L. Hall, and J. Ye, "Sub-Doppler molecular-iodine transitions near the dissociation limit (523–498 nm): errata," *Opt. Lett.* **27**, 1076–1076 (2002).
- J. Ye, L. S. Ma, and J. L. Hall, "Molecular iodine clock," *Phys. Rev. Lett.* **87**, 270801 (2001).
- R. J. Jones, W.-Y. Cheng, K. W. Holman, L. Chen, J. L. Hall, and J. Ye, "Absolute-frequency measurement of the iodine-based length standard at 514.67 nm," *Appl. Phys. B* **74**, 597–601 (2002).
- C. Ishibashi, J. Ye, and J. L. Hall, "Issues and applications in ultra-sensitive molecular spectroscopy," in *Methods for Ultrasensitive Detection II*, C. W. Wilkerson, Jr., ed., *Proc. SPIE* **4634**, 58–69 (2002).
- S. Gerstenkorn and P. Luc, *Atlas du Spectre d'Absorption de la Molécule d'Iode 14 800  $cm^{-1}$ –20 000  $cm^{-1}$*  (Editions u CNRS, Paris, 1985).
- F.-L. Hong, J. Ye, L.-S. Ma, S. Picard, C. J. Bordé, and J. L. Hall, "Rotation dependence of electric quadrupole hyperfine interaction in the ground state of molecular iodine by high-resolution laser spectroscopy," *J. Opt. Soc. Am. B* **18**, 379–387 (2001).
- J.-P. Wallerand, F. du Burck, B. Mercier, A. N. Goncharov, M. Himbert, and C. J. Bordé, "Frequency measurements of hyperfine splittings in ground rovibronic states of  $I_2$  by

- stimulated resonant Raman spectroscopy," *Eur. Phys. D* **6**, 63–76 (1999).
27. J. P. Pique, R. Bacis, M. Broyer, S. Churassy, and J. B. Koffend, "Calculation of the magnetic hyperfine interaction in the  $E$  and  $X$  states of iodine with the separated-atom theory," *J. Chem. Phys.* **80**, 1390–1393 (1984).
  28. S. Gerstenkorn, P. Luc, and C. Amiot, "Analysis of the long range potential of iodine in the  $B^3\Pi_{0u}^+$  state," *J. Phys. (Paris)* **46**, 355–364 (1985).
  29. P. J. Jewsbury, T. Ridley, K. P. Lawley, and R. J. Donovan, "Parity mixing in the valence states of  $I_2$  probed by optical-optical double-resonance excitation of ion-pair states—characterization of a new ion-pair state,  $H1_u(^3P_1)$ , and a valence state,  $c1_g$ ," *J. Mol. Spectrosc.* **157**, 33–49 (1993).
  30. T. J. Quinn, "Practical realization of the definition of the metre (1997)," *Metrologia* **36**, 211–244 (1999).
  31. F. L. Hong and J. Ishikawa, "Hyperfine structures of the  $R(122) 35-0$  and  $P(84) 33-0$  transitions of  $^{127}I_2$  near 532 nm," *Opt. Commun.* **183**, 101–108 (2000).
  32. C. S. Edwards, G. P. Barwood, P. Gill, F. Rodriguez Llorente, and W. R. C. Rowley, "Frequency-stabilised diode lasers in the visible region using Doppler-free iodine spectra," *Opt. Commun.* **132**, 94–100 (1996).
  33. C. S. Edwards, G. P. Barwood, P. Gill, and W. R. C. Rowley, "A 633 nm iodine-stabilized diode-laser frequency standard," *Metrologia* **36**, 41–45 (1999).
  34. A. Razet, J. Gagniere, and P. Juncar, "Hyperfine-structure analysis of the  $33P(6-3)$  line of  $^{127}I_2$  at 633 nm using a continuous-wave tunable dye-laser," *Metrologia* **30**, 61–65 (1993).
  35. H. R. Simonsen, "Iodine-stabilized extended cavity diode laser at  $\lambda = 633$  nm," *IEEE Trans. Instrum. Meas.* **46**, 141–144 (1997).
  36. A. Morinaga, K. Sugiyama, and N. Ito, "Hyperfine-structure of low-lying vibrational levels in the  $B$ -electronic state of molecular iodine," *J. Opt. Soc. Am. B* **6**, 1656–1659 (1989).
  37. P. Gill and J. A. Clancy, "A microprocessor-controlled iodine-stabilized ion laser," *J. Phys. E* **21**, 213–218 (1988).
  38. F. Bertinetto, P. Cordiale, S. Fontana, and G. B. Picotto, "Helium–neon lasers stabilized to iodine at 605-nm," *IEEE Trans. Instrum. Meas.* **36**, 609–612 (1987).
  39. W.-Y. Cheng, J. T. Shy, and T. Lin, "A compact iodine-stabilized HeNe laser and crossover resonances at 543 nm," *Opt. Commun.* **156**, 170–177 (1998).
  40. J. Vigué, M. Broyer, and J. C. Lehmann, "Natural hyperfine and magnetic predissociation of the  $I_2 B$  state. III. Experiments on magnetic predissociation," *J. Phys. (Paris)* **42**, 961–978 (1981).
  41. E. Martínez, M. T. Martínez, and F. Castano, "Iodine  $B^3\Pi_{0u}^+$  state predissociation—evaluation of the interaction mechanisms for predissociated levels of the  $B$ -state," *J. Mol. Spectrosc.* **128**, 554–563 (1988).
  42. V. Spirko and J. Blabla, "Nuclear-quadrupole coupling functions of the  $^1\Sigma_g^+$  and  $^3\Pi_{0u}^+$  states of molecular-iodine," *J. Mol. Spectrosc.* **129**, 59–71 (1988).
  43. W. S. Barney, C. M. Western, and K. C. Janda, "Measurement of the electronic wave function: separated atom wave function analysis of the  $R$ -dependent hyperfine constants of the iodine monochloride  $A$  state," *J. Chem. Phys.* **113**, 7211–7223 (2000).
  44. R. J. Le Roy, "LEVEL 7.5: A computer program for solving the radial Schrödinger equation for bound and quasibound levels," University of Waterloo Chemical Physics Research Rep. CP-655 (2002). The source code and manual for this program may be obtained from the Computer Programs link on the www site <http://leroy.uwaterloo.ca>.
  45. R. Bacis, M. Broyer, S. Churassy, J. Vergès, and J. Vigué, "eQq measurements in the  $X, 1_g, 0_g^+$ , and  $B$  state of  $I_2$ : a test of the electronic molecular eigenfunctions," *J. Chem. Phys.* **73**, 2641–2650 (1980).